

# XLES Part I: Introduction to Extended Large Eddy Simulation

Christoph Glawe<sup>a,c</sup>, Heiko Schmidt<sup>a</sup>, Alan R. Kerstein<sup>b</sup>, Rupert Klein<sup>c</sup>

<sup>a</sup>*BTU Cottbus-Senftenberg, Siemens-Halske-Ring 14, 03046 Cottbus, Germany*

<sup>b</sup>*72 Lomitas Road, Danville, CA 94526, USA*

<sup>c</sup>*FU Berlin, Arnimallee 6, 14195 Berlin, Germany*

---

## Abstract

Direct numerical simulation (DNS), mostly used in fundamental turbulence research, is limited to low turbulent intensities due the current and future computer resources. Standard turbulence models, like RaNS (Reynolds averaged Navier-Stokes) and LES (Large Eddy Simulation), are applied to flows in engineering, but they miss small scale effects, which are frequently of importance, see e.g. the whole area of reactive flows, flows with apparent Prandtl or Schmidt number effects, or even wall bounded flows. A recent alternative to these standard approaches is the one-dimensional turbulence (ODT) model, which is limited to 1D sub-domains. In two papers we will provide a generalized filter strategy, called XLES (extended LES), including a formal theory (part I) and one special approach in the XLES family of models, called ODTLES (in part II (see Glawe et al. (2015))). ODTLES uses an ODT sub-grid model to describe all turbulent scales not represented by XLES, which leaves the larger scales to be simulated in 3D. This allows a turbulence modeling approach with a 3D resolution mainly independent of the turbulent intensity. Thus ODTLES is able to compute highly turbulent flows in domains of moderate complexity affordably and including the full range of turbulent and diffusive scales. The convergence of XLES to DNS is shown and the unconventional XLES advection approach is investigated in basic numerical tests. In part II, highly turbulent channel and duct flow results are discussed and show the future potential of XLES and ODTLES.

*Keywords:*

---

*Email address:* Christoph.Glawe@protonmail.com (Christoph Glawe)

## 1. Introduction

Turbulence is a ubiquitous effect in the physical world, with major technological and environmental impacts on human society and even human existence. Turbulence influenced the density and associated gravity variations that led to the formation of present-day galaxies, stars, and planets. Without turbulent mixing, planetary atmospheric phenomena such as clouds, storms, and precipitation essential for life on Earth would be unimaginably different. Turbulence in the ocean has innumerable effects on oceanic biota, starting with the commingling of phytoplankton with needed nutrients. Due to its broad influence and baffling complexity, progress in fundamental and practical understanding of turbulent mixing is exceptionally challenging, yet crucial for scientific advancement encompassing a wide class of problems in earth science, astrophysics, and engineering. For such problems, better understanding of turbulence interactions with buoyancy effects and chemical and thermodynamic processes is equally important. Due to its huge complexity, progress in understanding and prediction of turbulence is extremely challenging, yet crucial for scientific advancement in many disciplines.

Analytic solutions of turbulent flows cannot be derived for real life applications, e.g. with complex boundary conditions. Many meteorological and technical turbulent flows are investigated by numerical simulations. However the theoretical analysis of the governing equations is important to derive and improve simplifying models.

There are several possible levels of turbulence modeling commonly applied. The simplest model is no model: Direct Numerical Simulation (DNS) resolves all turbulent scales. Thus impacts of modeling and numerical errors are not influencing the investigated physics. DNS is widely used in fundamental research, but limited to moderate Reynolds numbers  $Re$  (until now  $Re_\tau \approx 5200$  for wall-bounded flows by Lee and Moser (2014)) and Rayleigh numbers  $Ra$  due to the high computational effort, while many real-world flows have  $Re_\tau \gtrsim 10^6$  (following Smits and Marusic (2013)).

In many industrial and some research applications Reynolds-Averaged Navier-Stokes equations (RaNS equations) are solved, because highly turbulent flows (e.g.  $Re_\tau > 10^6$ ) corresponding to realistic flows are computationally feasible. RaNS describes the dynamics of time-averaged fields. The

influence of fluctuating terms is modeled. Various models are known (see e.g. Spalart and Allmaras (1992) or an overview by Pope (2000)). RaNS is used for steady states, but is generally not useful for computing time-accurate flow statistics.

In recent years, Large Eddy Simulation (LES) has increasingly been used for industrial applied and fundamental turbulent flows. In LES spatially filtered equations are numerically solved while the unresolved sub-grid scale (SGS) terms are modeled e.g. by an eddy viscosity model (see e.g. Germano et al. (1991)).

Even in very fundamental highly turbulent flows LES need to resolve a wide range of scales including at least some portion of the inertial range of the turbulent cascade, which limits the achievable Reynolds numbers relative to the achievable Reynolds numbers in RaNS simulations. The parameterization of a certain range of small scales in RaNS and LES is especially problematic for multi-physics regimes such as buoyant and reacting flows because much of the complexity is thus relegated to the unresolved small scales.

For further details on LES we refer to standard literature (e.g. by Sagaut (2006)). For an overview of turbulence properties and other model approaches we refer to the work by Pope (2000).

Alternative model approaches e.g. the one-dimensional turbulence (ODT) model (see e.g. Kerstein (1999) and Kerstein et al. (2001)) describe the 3D turbulence within a 1D sub-domain including the full turbulent cascade, whereby the numerical representation of molecular diffusive effects becomes computationally feasible also in highly turbulent flows. Recently Meiselbach (2015) described wall bounded flows with  $Re_\tau \leq 6 \times 10^5$  using an adaptive ODT version (by Lignell et al. (2013)), which is clearly in the range of real-world applications, but limited to applications that are reasonable within a 1D sub-domain.

To benefit from the ability of 1D models to describe highly turbulent flows, several approaches combine 1D models with LES, e.g. LES-ODT (e.g. by Cao and Echehki (2008)), LES/LEM (by Menon and Kerstein (2011)), and LEM3D (e.g. by Sannan et al. (2013)). Since ODT fully resolves e.g. molecular diffusion effects, it is fairly non-trivial to include it into an LES-like filter approach.

In this work we introduce an extended LES (XLES) filter approach, which is tailored to include 1D models as sub-grid models and can describe highly turbulent flows in a domain of moderate complexity, relevant e.g. in atmospheric science. To achieve this, XLES solves 2D filtered equations on a

structured grid, maintaining one highly resolved Cartesian direction (this e.g. allows resolved molecular diffusion within an ODT sub-grid model). To derive a preferably general model, all Cartesian directions are treated equally: Three 2D filters, each corresponding to one highly resolved Cartesian direction, are applied independently to the governing equation. This leads to three coupled sets of 2D filtered equations, derived in section 2.

Thereby XLES only needs to resolve global 3D structures (e.g. the computational domain) independent of the turbulent cascade, while e.g. a one-dimensional turbulence model oriented in the respective highly resolved directions efficiently exploits the special symmetry of a 2D filter and represents the XLES microscale terms, corresponding to turbulent velocity scales not resolved by XLES. This ODTLES approach, investigated in detail in part II (Glawe et al. (2015)), is beneficial for flows with turbulent small scale effects playing an important role, e.g. in the combustion area, in buoyant stratified flows and wall-bounded flows with high turbulent intensity e.g. with high Reynolds or Rayleigh numbers.

This XLES based ODTLES model is an extended version of the ODTLES model, introduced and examined by Schmidt et al. (2008), Gonzalez-Juez et al. (2011), and Glawe et al. (2013).

In this work we distinguish between the expressions XLES to describe the XLES approach including an approximation or model for arising microscale terms, ODTLES if these terms are in particular described by ODT and XLES-U (XLES unclosed), if microscale terms are neglected.

In this work the XLES approach is introduced (in section 2) and XLES-U is verified by numerical studies and applied to a turbulent channel flow (in section 3), followed by conclusions in section 4. In Part II (see Glawe et al. (2015)) ODTLES is derived as one special approach in the XLES family of models and highly turbulent ODTLES channel and duct flow results are presented.

Note that in this work no Einstein summation convention is used.

## 2. Extended Large Eddy Simulation (XLES)

We consider the turbulent flow to be described by the incompressible Navier-Stokes equations for a Newtonian fluid including the conservation of

mass in Eq. (1) and momentum in Eq. (2):

$$0 = \sum_{j=1}^3 \partial_{x_j} u_j \quad (1)$$

$$0 = \frac{1}{\rho_0} \partial_{x_i} p + \left[ \partial_t - \nu \sum_{j=1}^3 \partial_{x_j}^2 \right] u_i + \sum_{j=1}^3 \partial_{x_j} u_j \cdot u_i \quad (2)$$

with the velocity  $u_i$  in Cartesian  $x_i$ -direction ( $i = \{1, 2, 3\}$ ), a constant kinematic viscosity  $\nu$ , and the pressure gradient  $\partial_{x_i} p$ . For simplicity we assume in this work the constant density to be  $\rho_0 = 1$ .

Variables e.g. the velocities  $u_i$  and operators are assumed to be described within a continuum. Discrete variables are marked with the superscript  $d$  (e.g. discrete velocities:  $u_i^d$ ).

Similar to LES, in XLES the velocity field is filtered. 3D filter functions commonly applied in LES are defined as tensor products of 1D filter functions  $[l_k]$  (we are using an operator notation) in  $x_k$ -direction ( $k = \{1, 2, 3\}$ ; a filter operating on a continuum corresponds to a convolution). To derive macroscale (to be simulated) and microscale (to be modeled) terms the spatial scales are separated for modeling purpose using these 1D filter operators:

$$\begin{aligned} u_i &= [\mathbb{1} \mathbb{1} \mathbb{1}] u_i & (3) \\ &= [(l_1 + (\mathbb{1} - l_1))(l_2 + (\mathbb{1} - l_2))(l_3 + (\mathbb{1} - l_3))] u_i \\ &\equiv [(l_1 + s_1)(l_2 + s_2)(l_3 + s_3)] u_i \\ &= [l_1 l_2 l_3 + s_1 l_2 l_3 + l_1 s_2 l_3 + l_1 l_2 s_3 + s_1 s_2 l_3 + s_1 l_2 s_3 + l_1 s_2 s_3 + s_1 s_2 s_3] u_i \end{aligned}$$

with the unity operator  $[\mathbb{1}]$  and the 1D small scale operator

$$[s_k] = [\mathbb{1} - l_k]. \quad (4)$$

The tensor product ansatz causes combinations of 1D operators to be commutable, e.g.  $s_1 l_2 l_3 = l_3 s_1 l_2$ .

In general the occurring spatial 3D scales (terms in the last row of Eq. (3)) are decomposed into those to be simulated (resolved) and those to be modeled (unresolved). We will refer to this as ‘filter separation’, because the commonly used term ‘scale separation’ implies the simulated scales to be large. In LES the resolved velocities correspond to the 3D large scale field  $[l_1 l_2 l_3] u_i$ . Thus the LES filter separation corresponds to a 3D scale separation.

Table 1: Comparison of filter separation ansatzes

Model	resolved scales	unresolved scales (SGS)
LES	$\bar{u}_i^{\text{LES}} = [l_1 l_2 l_3] u_i$	$\tilde{u}_i^{\text{LES}} = [s_1 l_2 l_3 + l_1 s_2 l_3 + l_1 l_2 s_3 + s_1 s_2 l_3 + s_1 l_2 s_3 + l_1 s_2 s_3 + s_1 s_2 s_3] u_i$
DNS	$[\mathbb{1} \mathbb{1} \mathbb{1}] u_i$	0
XLES	$\bar{u}_i = [l_1 l_2 l_3 + s_1 l_2 l_3 + l_1 s_2 l_3 + l_1 l_2 s_3] u_i$	$\tilde{u}_i = [s_1 s_2 l_3 + s_1 l_2 s_3 + l_1 s_2 s_3 + s_1 s_2 s_3] u_i$

In table 1 the filter separations are compared between LES, DNS and XLES.

The LES resolved (large scale) velocities are  $\bar{u}_i^{\text{LES}} = [l_1 l_2 l_3] u_i$ , and the unresolved (SGS) velocities  $\tilde{u}_i^{\text{LES}} = [\mathbb{1} - l_1 l_2 l_3] u_i$ . The acronym LES is used to differentiate between standard LES velocities and those defined in XLES.

In DNS all available scales are resolved numerically.

In XLES the resolved scales are connected to 2D filtered fields. Without loss of generality (w.l.o.g.) we apply  $[l_1 l_2]$  leading to:

$$[l_1 l_2] u_i = [l_1 l_2 l_3 + l_1 l_2 s_3] u_i. \quad (5)$$

To treat all Cartesian directions equally, all possible 2D-filtered terms  $[l_2 l_3] u_i$ ,  $[l_1 l_3] u_i$ , and  $[l_1 l_2] u_i$  are resolved numerically.

This XLES macroscale (to be simulated) approach can be interpreted as the LES macroscale ( $[l_1 l_2 l_3]$ ) with additionally 1D resolved small scale (RSS) terms in all Cartesian directions ( $[s_1 l_2 l_3] + [l_1 s_2 l_3] + [l_1 l_2 s_3]$ ). Both, the XLES resolved velocity scales (investigated in this work) and the unresolved scales (investigated in part II (Glawe et al. (2015))) impose special requirements on the numerical scheme and modeling; techniques known from LES cannot be applied one-to-one to XLES.

### 2.1. XLES: Spatial Filtering

In XLES, 2D filter operators -each corresponding to one highly resolved Cartesian direction- are applied to the governing equations, comparable to the 3D filtering in LES. To derive a filter approach, independent of the chosen Cartesian direction, three 2D filters, corresponding to three Cartesian directions, are applied. We will use a vector notation (called XLES vector notation), indicated by an underbar (e.g.  $\underline{u}_i$ ). Each vector element contains

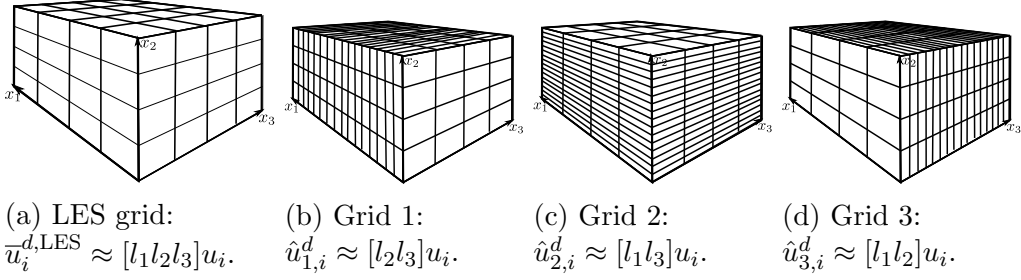


Figure 1: In XLES the velocities are resolved using multiple XLES-grids illustrated in 1b-1d. 3D large scale properties, corresponding to a standard LES grid are for illustration represented with  $N_{\text{LES}} = 4$  cells per direction in 1a. In XLES the 3D large scale velocities are derived by 1D filtering the XLES properties:  $\bar{u}_i^{\text{LES}} = [l_k] \hat{u}_{k,i}$ ,  $k = \{1, 2, 3\}$ . The discrete XLES resolved small scale ('RSS') properties are represented for illustration by  $N_{\text{RSS}} = 16$  cells in 1b-1d.

one of the three 2D filtered velocity fields:

$$\begin{pmatrix} [l_2 l_3] u_i \\ [l_1 l_3] u_i \\ [l_1 l_2] u_i \end{pmatrix} = \begin{pmatrix} l_2 l_3 & 0 & 0 \\ 0 & l_1 l_3 & 0 \\ 0 & 0 & l_1 l_2 \end{pmatrix} \begin{pmatrix} u_i \\ u_i \\ u_i \end{pmatrix} \equiv \underline{\underline{l}}^{2D} \underline{u}_i \equiv \hat{\underline{u}}_i \quad (6)$$

with the 2D filter matrix  $\underline{\underline{l}}^{2D}$ .

The 2D filtered velocity fields  $\hat{\underline{u}}_i$  (we refer to  $\hat{\underline{u}}_i$  as the XLES vector) are discretized using three overlapping staggered XLES-grids with face-centered velocities and cell-centered pressure, illustrated in figure 1b-1d, where each XLES-grid  $k = \{1, 2, 3\}$  discretizes one XLES vector element  $\hat{u}_{k,i}^d$ . The size of the discrete 1D filter  $[l_k^d]$  corresponds to the large scale cell size  $\Delta x_k^{\text{LES}}$  (see figure 1a), where the discrete 1D filter definition  $[l_k^d]$  corresponds to a box filter

$$[l_k^d] u_i = \frac{1}{\Delta x_k^{\text{LES}}} \int_{-\frac{\Delta x_k^{\text{LES}}}{2}}^{\frac{\Delta x_k^{\text{LES}}}{2}} u_i dx'_k. \quad (7)$$

Here the discrete mesh corresponds to the discrete filter size which is often called implicit filtering.

The XLES filter separation decomposes the full velocity field into three

parts (using the XLES vector notation):

$$\begin{aligned} \underline{u}_i &\equiv \begin{pmatrix} u_i \\ u_i \\ u_i \end{pmatrix} = \begin{pmatrix} [l_2 l_3] u_i \\ [l_1 l_3] u_i \\ [l_1 l_2] u_i \end{pmatrix} + \begin{pmatrix} [l_1 s_2 l_3 + l_1 l_2 s_3] u_i \\ [s_1 l_2 l_3 + l_1 l_2 s_3] u_i \\ [s_1 l_2 l_3 + l_1 s_2 l_3] u_i \end{pmatrix} + \begin{pmatrix} [\mathcal{S}] u_i \\ [\mathcal{S}] u_i \\ [\mathcal{S}] u_i \end{pmatrix} \\ &\equiv \underline{l}^{2D} \underline{u}_i + \underline{C} \underline{s}^{1D} \underline{l}^{2D} \underline{u}_i + [\mathcal{S}] \underline{u}_i : \end{aligned} \quad (8)$$

1. ‘Directly Resolved’:

The 2D filter  $\underline{l}^{2D}$  applied to the full velocity field leads to the XLES vector:  $\hat{u}_i = \underline{l}^{2D} \underline{u}_i$ . Each XLES-grid represents its own directly resolved velocity field distinct from the other XLES-grids.

2. ‘Indirectly Resolved’:

There are indirectly resolved small scale terms (‘directly resolved’ by another XLES-grid):  $\underline{C} \underline{s}^{1D} \underline{l}^{2D} \underline{u}_i$ . Especially within non-linear advection terms (in Eq. (2)), they determine the coupling between the XLES-grids. The coupling matrix  $\underline{C}$  and the small scale matrix  $\underline{s}^{1D}$  in Eq. (8) are:

$$\underline{C} = \begin{pmatrix} 0 & \mathbb{1} & \mathbb{1} \\ \mathbb{1} & 0 & \mathbb{1} \\ \mathbb{1} & \mathbb{1} & 0 \end{pmatrix} \quad \text{and} \quad \underline{s}^{1D} = \begin{pmatrix} s_1 & 0 & 0 \\ 0 & s_2 & 0 \\ 0 & 0 & s_3 \end{pmatrix}. \quad (9)$$

The matrix  $\underline{s}^{1D}$  defines the resolved small scale (RSS) velocities  $\check{u}_i$  (these are part of the XLES macroscale, contrary to LES):

$$\underline{s}^{1D} \underline{u}_i \equiv \check{u}_i = \hat{u}_i - \underline{l}^{1D} \hat{u}_i = \hat{u}_i - \underline{u}_i^{\text{LES}} \quad (10)$$

with the 1D filter matrix

$$\underline{l}^{1D} = \begin{pmatrix} l_1 & 0 & 0 \\ 0 & l_2 & 0 \\ 0 & 0 & l_3 \end{pmatrix}. \quad (11)$$

In index notation: The term (w.l.o.g.)  $[l_1 s_2 l_3] u_i = [l_1 l_3] u_i - [l_1 l_2 l_3] u_i$  can be interpreted numerically, because  $\hat{u}_{2,i} = [l_1 l_3] u_i$  is exclusively available in XLES-grid 2 and the 1D filtered XLES velocity field  $[l_2] \hat{u}_{2,i} = [l_1 l_2 l_3] u_i$ , corresponding to the LES velocity field  $\bar{u}_i^{\text{LES}}$  (see figure 1), is also available in XLES-grid 2.



3. ‘Not Resolved’:

The velocity scales  $[\mathcal{S}]u_i = [s_1s_2l_3 + s_1l_2s_3 + l_1s_2s_3 + s_1s_2s_3]u_i$  are not resolved in any XLES-grid (XLES sub-grid scale (SGS) or XLES microscale). In part II (Glawe et al. (2015)) advection terms containing unresolved velocity scales are interpreted by the ODT model.

We summarize all resolved velocity scales (directly and indirectly):

$$\underline{\bar{u}}_i = [l_1l_2l_3 + s_1l_2l_3 + l_1s_2l_3 + l_1l_2s_3]\underline{u}_i = (\underline{l}^{2D} + \underline{\underline{C}}\underline{\underline{s}}^{1D}\underline{l}^{2D})\underline{u}_i. \quad (12)$$

A possible interpretation of the XLES macroscale is the numerical approximation of  $\underline{\bar{u}}_i$  instead of  $\bar{u}_i^{\text{LES}} = [l_1l_2l_3]u_i$  in LES (compare to table 1). Appendix A shows that expressing  $\underline{\bar{u}}_i$  in index notation automatically leads to three coupled XLES-grids (corresponding to Eq. (12)).

## 2.2. Momentum Conservation

Similar to LES, in XLES filtered equations are solved. Contrary to LES the XLES equations are derived by applying a 2D filter matrix  $\underline{l}^{2D}$  to the momentum equation Eq. (2) leading to (in XLES vector notation):

$$0 = \partial_{x_i}\hat{p} + \left( \partial_t - \nu \sum_{j=1}^3 \partial_{x_j}^2 \right) \hat{u}_i + \sum_{j=1}^3 \partial_{x_j} \hat{u}_j * \hat{u}_i + \sum_{j=1}^3 \tau_{ij}^{\text{XLES}} \quad (13)$$

with the 2D filtered pressure

$$\hat{p} = \underline{l}^{2D} p = ([l_2l_3]p \ [l_1l_3]p \ [l_1l_2]p)^T, \quad (14)$$

the XLES residual stress tensors  $\tau_{ij}^{\text{XLES}}$ , and the Hadamard operator  $*$ , an entry-wise multiplication between XLES vectors and matrices.

The three 2D filtered momentum equations, each describing three velocity components (hence the number of equations is tripled), coexist and are solved simultaneously.

Compared to LES advection terms  $\partial_{x_j} \bar{u}_j^{\text{LES}} \bar{u}_i^{\text{LES}}$  the XLES advection terms  $\partial_{x_j} \hat{u}_j * \hat{u}_i = \partial_{x_j} (\underline{\bar{u}}_j^{\text{LES}} + \tilde{u}_j) * (\underline{\bar{u}}_i^{\text{LES}} + \tilde{u}_i)$  contain additional XLES-grid specific resolved small scale (RSS) terms.

The contribution associated with the XLES residual stress tensors

$$\tau_{ij}^{\text{XLES}} = \underline{l}^{2D} (\partial_{x_j} \underline{u}_j * \underline{u}_i) - \partial_{x_j} \hat{u}_j * \hat{u}_i \quad (15)$$

is captured through the use of some form of modeling or approximation. To investigate the residual stresses in more detail, a 2D decomposition (a modified version of the 3D decomposition by Leonard (1975)) is performed, leading to:

$$\underline{\tau}_{ij}^{\text{XLES}} = \underline{\mathcal{X}}_{ij}^{\text{XLES}} + \underline{\mathcal{L}}_{ij}^{2D} + \underline{\mathcal{C}}_{ij}^{\text{XLES}} + \underline{\mathcal{R}}_{ij}^{\text{XLES}} \quad (16)$$

where:

- XLES coupling tensor terms

$$\underline{\mathcal{X}}_{ij}^{\text{XLES}} = \partial_{x_j} (\hat{u}_j * \underline{\underline{C}}_{\underline{\underline{s}}}^{1D} \underline{\underline{l}}^{2D} \underline{u}_i + \underline{\underline{C}}_{\underline{\underline{s}}}^{1D} \underline{\underline{l}}^{2D} \underline{u}_j * \hat{u}_i + \underline{\underline{C}}_{\underline{\underline{s}}}^{1D} \underline{\underline{l}}^{2D} \underline{u}_j * \underline{\underline{C}}_{\underline{\underline{s}}}^{1D} \underline{\underline{l}}^{2D} \underline{u}_i) \quad (17)$$

involve ‘indirectly resolved’ terms. These stress terms couple the momentum equations represented by different XLES-grids. A possible approximation of  $\underline{\mathcal{X}}_{ij}^{\text{XLES}}$  is investigated in section 2.2.1. In LES these terms are not simulated and therefore typically modeled or approximated and contribute to 3D cross-stress and 3D SGS Reynolds stress terms.

- 2D Leonard stresses

$$\underline{\mathcal{L}}_{ij}^{2D} = (\underline{\underline{l}}^{2D} \partial_{x_j} (\hat{u}_j * \hat{u}_i) - \partial_{x_j} \hat{u}_j * \hat{u}_i) + (\underline{\underline{l}}^{2D} \underline{\mathcal{X}}_{ij}^{\text{XLES}} - \underline{\mathcal{X}}_{ij}^{\text{XLES}}) \quad (18)$$

describe the influence of the 2D filter on the (‘directly’ and ‘indirectly’) resolved XLES advection terms (see section 2.2.2 for details).

- XLES cross-stress terms

$$\underline{\mathcal{C}}_{ij}^{\text{XLES}} = \underline{\underline{l}}^{2D} \partial_{x_j} (\tilde{u}_j * \hat{u}_i + \hat{u}_j * \tilde{u}_i) + \underline{\underline{l}}^{2D} \partial_{x_j} (\tilde{u}_j * \underline{\underline{C}}_{\underline{\underline{s}}}^{1D} \underline{\underline{l}}^{2D} \underline{u}_i + \underline{\underline{C}}_{\underline{\underline{s}}}^{1D} \underline{\underline{l}}^{2D} \underline{u}_j * \tilde{u}_i) \quad (19)$$

describe the interaction of resolved (‘directly’ and ‘indirectly’) and unresolved XLES terms (see section 2.2.2 for details).

- 2D SGS Reynolds stresses

$$\underline{\mathcal{R}}_{ij}^{\text{XLES}} = \underline{l}^{2D} \partial_{x_j} (\underline{\tilde{u}}_j * \underline{\tilde{u}}_i) \quad (20)$$

describe the interaction of terms not resolved in XLES (see section 2.2.2 for details).

The XLES stress terms  $\underline{\mathcal{L}}_{ij}^{2D}$ ,  $\underline{\mathcal{C}}_{ij}^{\text{XLES}}$ , and  $\underline{\mathcal{R}}_{ij}^{\text{XLES}}$  are investigated in more detail in section 2.2.2 and can be interpreted in the context of the ODT model, as shown in part II (see Glawe et al. (2015)).

A 2D decomposition following the idea of Germano (1986) is also possible within the XLES framework. Nevertheless the 2D decomposition following Leonard (1975) is sufficient to introduce ODT into the XLES framework and therefore used here in preparation for part II (Glawe et al. (2015)).

### 2.2.1. XLES: Resolved Advection Terms

The coupling stress terms  $\underline{\mathcal{X}}_{ij}^{\text{XLES}}$  in Eq. (17) are decomposed into two terms (using  $\underline{\tilde{u}}_i$  from Eq. (10)):

$$\underline{\mathcal{X}}_{ij}^{\text{XLES}} = (\underline{\underline{C}} \partial_{x_j} (\underline{\hat{u}}_j * \underline{\hat{u}}_i - \underline{\bar{u}}_j^{\text{LES}} * \underline{\bar{u}}_i^{\text{LES}}))^T + \partial_{x_j} (\underline{\underline{1}} \underline{\tilde{u}}_j * \underline{\underline{1}} \underline{\tilde{u}}_i - \underline{\underline{1}} (\underline{\tilde{u}}_j * \underline{\tilde{u}}_i)) \quad (21)$$

with the matrix of ones  $\underline{\underline{1}}$  and where:

1. The first term in Eq. (21) exclusively contains advection terms with advecting and advected velocities represented within the same XLES-grid. This can be interpreted as a linearization affecting the coupling, while the individual advection terms  $\partial_{x_j} \hat{u}_{k,j} \hat{u}_{k,i}$  and  $\partial_{x_j} \bar{u}_{k,j}^{\text{LES}} \bar{u}_{k,i}^{\text{LES}}$  in each XLES-grid  $k$  remain non-linear. We investigate w.l.o.g. one element of a transposed coupling vector  $(\underline{\underline{C}} \partial_{x_j} \hat{u}_j * \hat{u}_i)^T$  in detail: For XLES-grid 1 we find e.g.

$$\partial_{x_j} ([l_1 l_3] u_j [l_1 l_3] u_i) \quad (22)$$

with the velocities  $[l_1 l_3] u_j = \hat{u}_{2,j}$  ( $j = \{1, 2, 3\}$ ) only discretely represented in XLES-grid 2.

This transposed coupling vector can be rearranged:

$$(\underline{\underline{C}} \partial_{x_j} \hat{u}_j * \hat{u}_i)^T = \underline{\underline{l}}^\dagger * \underline{\underline{C}} \partial_{x_j} \hat{u}_j * \hat{u}_i \quad (23)$$

with the matrix

$$\underline{\underline{l}}^\dagger = \begin{pmatrix} \mathbb{1} & l_1^{-1}l_2 & l_1^{-1}l_3 \\ l_2^{-1}l_1 & \mathbb{1} & l_2^{-1}l_3 \\ l_3^{-1}l_1 & l_3^{-1}l_2 & \mathbb{1} \end{pmatrix}. \quad (24)$$

Using Eq. (23) the same example in Eq. (22) leads to:

$$[l_1^{-1}][l_2]\partial_{x_j}([l_1l_3]u_j [l_1l_3]u_i) \quad (25)$$

which is computed in XLES-grid 2 and then coupled to XLES-grid 1. Eq. (24) contains deconvolution operators  $[l_k^{-1}]$ , which are realizable if only large scale information is present. This is the case in XLES: the velocities  $[l_1l_3]u_j$  and  $[l_1l_3]u_i$  in the example in Eq. (25) are large scale in the  $x_1$ -direction, which is the direction of the deconvolution. This implies that Eq. (23) is exact for a continuum.

A discrete (numerical) approximation  $\underline{\underline{l}}^{\dagger a} \approx \underline{\underline{l}}^\dagger$  is provided by the algorithm shown in section 3.1.

Using the matrix  $\underline{\underline{l}}^\dagger$  (including deconvolutions) the linearized coupling stress terms are:

$$\underline{\underline{\mathcal{X}}}_{ij}^{XLES} = \underline{\underline{l}}^\dagger * \underline{\underline{C}} \partial_{x_j} (\hat{u}_j * \hat{u}_i - \bar{u}_j^{LES} * \bar{u}_i^{LES}). \quad (26)$$

2. The second term in Eq. (21) can be expanded as follows:

$$\begin{aligned} & \partial_{x_j} (\underline{\underline{1}} \check{u}_j * \underline{\underline{1}} \check{u}_i - \underline{\underline{1}}(\check{u}_j * \check{u}_i)) \\ & = \partial_{x_j} \underline{\underline{1}}(\check{u}_{1,j} \check{u}_{2,i} + \check{u}_{1,j} \check{u}_{3,i} + \check{u}_{2,j} \check{u}_{1,i} + \check{u}_{2,j} \check{u}_{3,i} + \check{u}_{3,j} \check{u}_{1,i} + \check{u}_{3,j} \check{u}_{2,i}). \end{aligned} \quad (27)$$

These terms contain interactions of small-scale velocities resolved in different XLES-grids. We neglect these non-linear coupling terms. For an intact energy cascade within the turbulent flow this assumption is reasonable because it implies that the velocities  $\check{u}_{k,j} = \hat{u}_{k,j} - \bar{u}_{k,j}^{LES}$  are smaller than  $\hat{u}_{k,j}$ .

The deconvolution within the coupling terms Eq. (26) is fundamentally different in XLES than in existing filtered treatments that do not have resolved small scales. The reason is that the deconvolution in XLES is not intended to construct small-scale features that are otherwise non-existent, but rather, to modify a small-scale structure that already exists at the resolved small scales, recognizing that this structure also has low-wavenumber

content. Indeed, the goal in principle is to modify appropriately that low-wavenumber content while preserving the high-wavenumber content to the greatest possible extent (see the example in Appendix C.3).

By neglecting the non-linear coupling terms a XLES model error is introduced:

$$\underline{\sigma}_{\text{XLES}}^{\text{spatial}} = \partial_{x_j} \left( \underline{1} \tilde{u}_j * \underline{1} \tilde{u}_i - \underline{1} (\tilde{u}_j * \tilde{u}_i) \right). \quad (28)$$

In LES-U (unclosed LES), the LES-limit of XLES-U (see section 3.2), the model error  $\underline{\sigma}_{\text{XLES}}^{\text{spatial}}$  vanishes and thus comparing a convergence study of XLES-U and LES-U in section 3.4) allows estimation of  $\underline{\sigma}_{\text{XLES}}^{\text{spatial}}$ .

### 2.2.2. XLES-SGS: Leonard Stress, Cross-Stress and SGS Reynolds Stress Terms

In this section the (to be modeled) stress tensors containing XLES microscale (unresolved) terms  $\underline{\tau}_{ij}^{\text{XLES}} - \underline{\mathcal{X}}_{ij}^{\text{XLES}} = \underline{\mathcal{L}}_{ij}^{2D} + \underline{\mathcal{C}}_{ij}^{\text{XLES}} + \underline{\mathcal{R}}_{ij}^{\text{XLES}}$  are investigated:

- The Leonard stresses  $\underline{\mathcal{L}}_{ij}^{2D} = \underline{l}^{2D} \partial_{x_j} (\hat{u}_j * \hat{u}_i + \underline{\mathcal{X}}_{ij}^{\text{XLES}}) - \partial_{x_j} (\hat{u}_j * \hat{u}_i + \underline{\mathcal{X}}_{ij}^{\text{XLES}})$  can in principle be calculated by explicit filtering of the directly and indirectly resolved XLES advection terms.

The 2D Leonard stresses are expected to be small within a discrete formulation, since each 2D filter size matches the corresponding XLES-grid size, similar to implicit filtering in LES.

Ferziger and Peric (1999) (and authors therein) report that explicit filtering the LES advection terms produces immoderate dissipation and neglecting the 3D Leonard stresses improves the outcome.

According to these arguments we neglect  $\underline{\mathcal{L}}_{ij}^{2D}$ .

Other attempts to model the 3D Leonard stresses are not transferred to the 2D Leonard stresses in this work.

- The cross-stress  $\underline{\mathcal{C}}_{ij}^{\text{XLES}}$  and SGS Reynolds stress terms  $\underline{\mathcal{R}}_{ij}^{\text{XLES}}$  describe interactions including the XLES unresolved scales  $\tilde{u}_i = [\mathcal{S}]u_i$  (see table 1). These terms can be modeled (e.g. by ODT).

We decompose these stress terms:

$$\begin{aligned} \underline{\mathcal{C}}_{ij}^{\text{XLES}} + \underline{\mathcal{R}}_{ij}^{\text{XLES}} = & \partial_{x_j} (\underline{l}^{2D} + \underline{l}^\dagger * \underline{C} \underline{l}^{2D}) (\tilde{u}_j * \tilde{u}_i + \tilde{u}_j * \tilde{u}_i) \\ & + \partial_{x_j} (\underline{l}^{2D} \quad \quad \quad) (\tilde{u}_j * \tilde{u}_i^{\text{LES}} + \tilde{u}_j^{\text{LES}} * \tilde{u}_i + \tilde{u}_i * \tilde{u}_j) \end{aligned} \quad (29)$$

into:

1. The terms  $\partial_{x_j} (\underline{l}^{2D} + \underline{l}^\dagger * \underline{C} \underline{l}^{2D}) (\tilde{u}_j * \tilde{u}_i + \tilde{u}_j * \tilde{u}_i)$  depend on the resolved small scale velocities  $\tilde{u}_j$  exclusively available in one XLES-grid.
2. The terms  $\partial_{x_j} \underline{l}^{2D} (\tilde{u}_j * \underline{u}_i^{\text{LES}} + \underline{u}_j^{\text{LES}} * \tilde{u}_i + \tilde{u}_i * \tilde{u}_j)$  are independent of the XLES-grid (equal in all XLES-grids). If a modeling approach is simultaneously applied in different XLES-grids, a SGS-coupling is required to guarantee a consistent 3D large scale field. Ad hoc introduction of an additional coupling, e.g.  $(\underline{l}^{2D} + \underline{l}^\dagger * \underline{C} \underline{l}^{2D}) (\tilde{u}_j * \underline{u}_i^{\text{LES}} + \underline{u}_j^{\text{LES}} * \tilde{u}_i + \tilde{u}_i * \tilde{u}_j)$ , would lead to double counting of small scale terms available in all XLES-grids. Nevertheless the exact relation

$$\begin{aligned} & \underline{l}^{2D} (\tilde{u}_j * \underline{u}_i^{\text{LES}} + \underline{u}_j^{\text{LES}} * \tilde{u}_i + \tilde{u}_i * \tilde{u}_j) \\ &= \frac{1}{3} (\underline{l}^{2D} + \underline{l}^\dagger * \underline{C} \underline{l}^{2D}) (\tilde{u}_j * \underline{u}_i^{\text{LES}} + \underline{u}_j^{\text{LES}} * \tilde{u}_i + \tilde{u}_i * \tilde{u}_j). \end{aligned} \quad (30)$$

avoids double counting due to the factor  $\frac{1}{3}$  (proof of  $\underline{l}^{2D} = \frac{1}{3} (\underline{l}^{2D} + \underline{l}^\dagger * \underline{C} \underline{l}^{2D})$  by insertion).

We reformulate and summarize the XLES microscale terms in Eq. (29):

$$\underline{C}_{ij}^{\text{XLES}} + \underline{R}_{ij}^{\text{XLES}} = (\underline{l}^{2D} + \underline{l}^\dagger * \underline{C} \underline{l}^{2D}) \underline{M}_{ij} \quad (31)$$

with

$$\underline{M}_{ij} = \partial_{x_j} \left( \tilde{u}_j * \tilde{u}_i + \tilde{u}_j * \tilde{u}_i + \frac{1}{3} (\tilde{u}_j * \underline{u}_i^{\text{LES}} + \underline{u}_j^{\text{LES}} * \tilde{u}_i + \tilde{u}_i * \tilde{u}_j) \right). \quad (32)$$

Each vector element  $\underline{M}_{k,ij}$  contains the unresolved terms (SGS) in XLES-grid  $k$  which are coupled to the other XLES-grids by the SGS coupling terms  $\underline{l}^\dagger * \underline{C} \underline{l}^{2D} \underline{M}_{ij}$ .

Summarizing section 2.2.1 and 2.2.2 we can write the XLES momentum equations:

$$\begin{aligned}
0 = & \partial_{x_i} \hat{p} + \left( \partial_t - \nu \sum_{j=1}^3 \partial_{x_j}^2 \right) \hat{u}_i + \sum_{j=1}^3 \partial_{x_j} \hat{u}_j * \hat{u}_i + \underline{\sigma}_{XLES}^{\text{spatial}} \\
& + \sum_{j=1}^3 \left( \underline{l}^{2D} \underline{\mathcal{M}}_{ij} \right) + \underline{\sigma}_{SGS}^{\text{spatial}} \\
& + \sum_{j=1}^3 \left( \underline{l}^\dagger * \underline{C} \partial_{x_j} (\hat{u}_j * \hat{u}_i - \underline{u}_j^{\text{LES}} * \underline{u}_i^{\text{LES}}) + \underline{l}^\dagger * \underline{C} \underline{l}^{2D} \underline{\mathcal{M}}_{ij} \right).
\end{aligned} \tag{33}$$

The last line in Eq. (33) corresponds to the full coupling, including the SGS terms and the indirectly resolved terms.

Additionally to the error term  $\underline{\sigma}_{XLES}^{\text{spatial}}$  in Eq. (28) neglecting the Leonard stresses introduces the SGS error term:

$$\underline{\sigma}_{SGS}^{\text{spatial}} = \underline{\mathcal{L}}_{ij}^{2D}. \tag{34}$$

Please note at this stage no concrete SGS model is introduced to approximate  $\underline{\mathcal{M}}_{ij}$ .

### 2.2.3. XLES: Mass Conservation

In the incompressible flow regime, the filtered velocity fields need to be divergence free to ensure mass conservation.

The 2D filter matrix  $\underline{l}^{2D}$  is applied to the mass conservation equation Eq. (1) (in the XLES vector notation):

$$0 = \sum_{i=1}^3 \partial_{x_i} \underline{l}^{2D} \underline{u}_i = \sum_{i=1}^3 \partial_{x_i} \underline{u}_i^{\text{LES}} + \sum_{i=1}^3 \partial_{x_i} \check{u}_i \tag{35}$$

which is decomposed into 3D large scale velocity fields  $\underline{u}_i^{\text{LES}}$  and resolved small scale (RSS) velocities  $\check{u}_i$ .

A possible approach to solve Eq. (35) is to ensure mass conservation for both decomposed velocity fields  $\underline{u}_i^{\text{LES}}$  and  $\check{u}_i = \underline{s}^{1D} \underline{u}_i$ :

1. The equation  $0 = \sum_{i=1}^3 \partial_{x_i} \underline{u}_i^{\text{LES}}$  corresponds to the mass conservation in LES schemes. Standard discrete approaches applied in LES can be used. In our implementation a

pressure Poisson equation is solved. This leads to a large scale pressure field  $\bar{p}^{\text{LES}} = \underline{l}^{3D} p$ , whose gradient enforces a divergence free velocity field  $\bar{u}_i^{\text{LES}}$  by solving  $\partial_t \bar{u}_i^{\text{LES}} + \partial_{x_i} \bar{p}^{\text{LES}} = 0$  (for details we refer to standard textbooks, e.g. Ferziger and Peric (1999)).

2. The equation  $0 = \sum_{i=1}^3 \partial_{x_i} \check{u}_i$ , corresponding to the RSS velocity fields, is discretely fulfilled without additional effort under some conditions.

In Appendix B the XLES mass conservation is derived in detail and three conditions are identified to ensure the RSS velocities to be divergence free:

- Consistency condition:  $\bar{u}_{k,i}^{\text{LES}}$  is equal in all XLES-grids  $k$  which is valid due to coupling (see section 3.2 for details).
- A divergence free 3D large scale velocity field which is valid after the standard pressure projection.
- A discrete 1D box filter defined in Eq. (7) is used. Here we introduce a coarse-grained (large scale) and staggered control volume of the size  $\Delta x_k^{\text{LES}}$  (this cell size equals the filter size). Please note this filter definition is only used explicitly to create  $\bar{u}_i^{\text{LES}} = [l_k] \hat{u}_{k,i}$  within the coupling and the mass conservation. The 2D filter  $\underline{l}^{2D}$  is not applied explicitly to any term.

In summary the discrete mass conservation is assured by a standard 3D approach (large scale) with  $\mathcal{O}(N_{\text{LES}}^3)$  cells, if a box filter and a staggered grid is used.

In XLES the velocity fields, including consistent 3D large scale informations, are discretely interpreted in three XLES-grids simultaneously. For such a system an existing redundancy of the discrete velocity fields can be exploited by deriving the velocity components  $\hat{u}_{k,k}^d$  within one 3D large scale cell due to a direct solution, w.l.o.g. in XLES-grid 1:

$$\hat{u}_{1,1}^d \left( \frac{-\Delta x_1^{\text{LES}}}{2} + x_1 \right) = \bar{u}_1^{d, \text{LES}} \left( -\frac{\Delta x_1^{\text{LES}}}{2} \right) \quad (36)$$

$$- \int_{-\frac{\Delta x_1^{\text{LES}}}{2}}^{\frac{\Delta x_1^{\text{LES}}}{2} + x_1} \partial_{x_2} \hat{u}_{1,2}^d dx'_1 - \int_{-\frac{\Delta x_1^{\text{LES}}}{2}}^{\frac{\Delta x_1^{\text{LES}}}{2} + x_1} \partial_{x_3} \hat{u}_{1,3}^d dx'_1$$

for  $x_1 \leq \Delta x_1^{\text{LES}}$ . Eq. (36) is a semi discrete interpretation of Gauss's theorem for a divergence free velocity field tailored for velocities in XLES-grid 1 (see



figure 1b) within one 3D large scale cell (see figure 1a) on a staggered face centered grid (no interpolation necessary).

Since w.l.o.g.  $\hat{u}_{1,1}$  is specified due to Eq. (36), the momentum equation Eq. (33) in XLES-grid 1 only needs to be solved for  $i = \{2, 3\}$ . In consequence 6 momentum equations are dynamically solved (2 velocity components in each of 3 XLES-grids), while 3 velocity components can be derived by Eq. (36).

These reduced momentum equations can be expressed by multiplying a Kronecker delta operator matrix

$$\underline{\underline{1}} - \underline{\underline{\delta}}_i = \begin{pmatrix} 1 - \delta_{1i} & 0 & 0 \\ 0 & 1 - \delta_{2i} & 0 \\ 0 & 0 & 1 - \delta_{3i} \end{pmatrix}, \text{ with } (1 - \delta_{ki}) = \begin{cases} 0, & \text{if } k = i \\ 1, & \text{else} \end{cases} \quad (37)$$

giving:

$$\begin{aligned} 0 = & (\underline{\underline{1}} - \underline{\underline{\delta}}_i) \left( \partial_{x_i} \bar{p}^{\text{LES}} + \left( \partial_t - \nu \sum_{j=1}^3 \partial_{x_j}^2 \right) \hat{u}_i + \sum_{j=1}^3 \partial_{x_j} \hat{u}_j * \hat{u}_i \right) \\ & + (\underline{\underline{1}} - \underline{\underline{\delta}}_i) \left( \sum_{j=1}^3 (\underline{\underline{l}}^\dagger * \underline{\underline{C}} \partial_{x_j} (\hat{u}_j * \hat{u}_i - \bar{u}_j^{\text{LES}} * \bar{u}_i^{\text{LES}})) \right) + (\underline{\underline{1}} - \underline{\underline{\delta}}_i) \sigma^{\text{spatial}} \\ & + (\underline{\underline{1}} - \underline{\underline{\delta}}_i) \sum_{j=1}^3 (\underline{\underline{l}}^{2D} \underline{\underline{M}}_{ij}) + (\underline{\underline{1}} - \underline{\underline{\delta}}_i) \sum_{j=1}^3 (\underline{\underline{l}}^\dagger * \underline{\underline{C}} \underline{\underline{l}}^{2D} \underline{\underline{M}}_{ij}). \end{aligned} \quad (38)$$

Please note the Kronecker delta operator matrix is also applied to the unresolved terms  $\underline{\underline{M}}_{ij}$  and therefore can be exploited within a model approach. Additionally the factor  $\frac{1}{3}$  within Eq. (32) can be replaced by  $\frac{1}{2}$ .

Since in XLES no 3D small scale velocity field is defined, small scale pressure effects can only be captured by the modeling approach (additionally to the modeling of the SGS advection terms  $\underline{\underline{M}}_{ij}$ ).

### 3. Properties of the XLES Approach

#### 3.1. XLES: Deconvolution

In sections 2.2.1 and 2.2.2 coupling terms between the XLES-grids are introduced. A discrete approximation of the transposed coupling matrix  $(\underline{\underline{C}} \underline{\underline{l}}^{2D})^T = \underline{\underline{l}}^\dagger * \underline{\underline{C}} \underline{\underline{l}}^{2D}$  is required to numerically represent these coupling terms.

Within the matrix  $\underline{l}^\dagger$  (see Eq. (24)) an discrete deconvolution operator  $[l_k^{-1d}]$  has to be interpreted.

In general a velocity field  $u$  (indices are skipped in this section and all variables are assumed to be discrete representations) cannot be reconstructed exactly ( $[l^{-1}l] \neq 1$ ), because by filtering (e.g.  $u^{\text{LES}} = [l]u$ ) information get lost. This is not recoverable, unless only large scale information is present in the full spectrum, which is fortunately the case in XLES, as shown by an example in Eq. (25).

The deconvolution within XLES is not intended to construct small-scale features, but rather, to modify the low-wavenumber content of an existing fully resolved property. This modification must meet several requirements:

- Integral constraints are imposed to satisfy conservation laws at the level of the individual 3D coarse-grained cells. This means the box filtered large scale field needs to be preserved by the deconvolution, e.g. to enable the consistency preservation of the 3D velocity field required for the mass conservation and the LES limit of the XLES model (in section 3.2):

$$[l][l^{-1}] = 1. \tag{39}$$

- The deconvolution must in some sense modify the large scale structure along the resolved direction while in some sense preserving the small-scale structure. In this sense this deconvolution is a reconstruction of existing structure rather than a construction of something that does not otherwise exist. For this reason the term reconstruction has been used to describe it (Schmidt et al. (2008) and McDermott (2005)).

In principle the deconvolution approach is not restricted to one particular filter definition (e.g. spectral filter, box filter, Gaussian filter), but the mass conservation is greatly simplified if a box filter is used, as shown in Appendix B.

In this section we introduce a discrete approximation of the deconvolution operator  $[l^{-1}]$  for the purpose of computing a highly resolved velocity field  $u_a \approx [l^{-1d}]u^{\text{LES}}$  ( $a$  indicates an approximation by discretely interpreting  $[l^{-1}]$ ) from a box filtered field  $u^{\text{LES}} = [l]u$ .

Schmidt et al. (2008) introduces a recursive and very fast algorithm approximating  $u_a \approx [l^{-1}]u^{\text{LES}}$  with 8th order accuracy without changing the

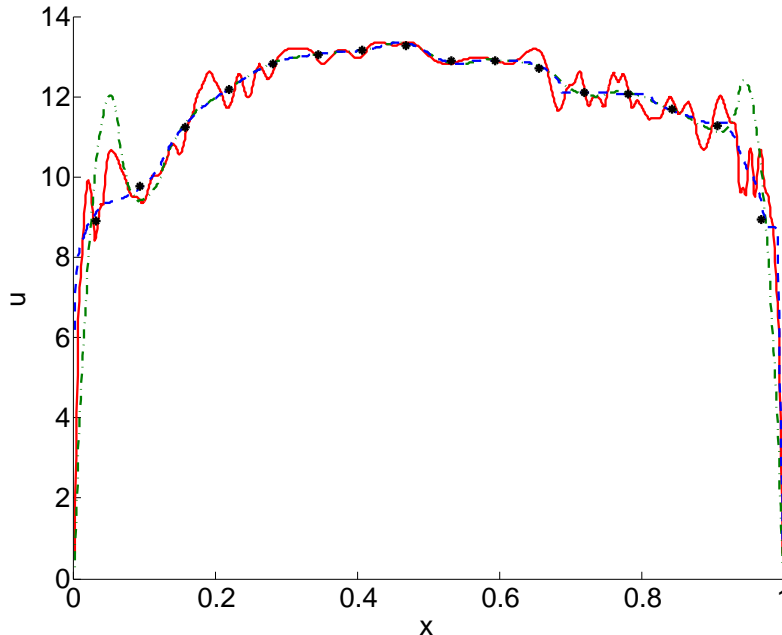


Figure 2: A representative instantaneous streamwise velocity profile  $u$  (solid) for a turbulent channel ( $Re_\tau = 1020$ ) with  $N_{LES} = 16$  and  $N_{RSS} = 1024$  is shown. The large scale velocity  $u^{LES} = [l]u$  is represented with points. The deconvolution  $u_a \approx [l^{-1}]u^{LES}$  using the original algorithm by Schmidt et al. (2008) is dashed-dotted and the limited algorithm is dashed. For both algorithms (limited and unlimited) the reconstructed field  $u_a$  preserves the box-filtered values  $[l]u_a = u^{LES}$ , but without the limiter unphysical overshoots occur near the walls.

box filtered field ( $[l]u_a = u^{LES} \equiv [l]u$ , see Eq. (39)). For algorithmic details, we refer to Schmidt et al. (2008), Gonzalez-Juez et al. (2011), and McDermott (2005).

The algorithm produces artificial local extrema in areas of monotone large scale fields with large gradients, e.g. occurring near a wall as reported by McDermott (2005). Similar effects are known from deconvolution approaches within the fields of image and signal processing. We expand this algorithm by applying the linear slope limiter by Burbeau et al. (2001) after each recursive step in the area of monotone velocities. Hereby monotonicity is defined locally for one cell by including its neighbors.

The properties of the original algorithm and the limited one are demon-

strated for a realistic instantaneous streamwise velocity profile  $u$  for a turbulent channel case with high gradients at the walls, shown in Figure 2 (please note in XLES only large scale information is deconvolved).

The numerical deconvolution error due to the algorithm described can be written formally:

$$\underline{\underline{\sigma}}_a^{\text{spatial}} = (\underline{\underline{l}}^\dagger * \underline{\underline{C}} - \underline{\underline{l}}^{\dagger a} * \underline{\underline{C}}) (\partial_{x_j} (\hat{u}_j * \hat{u}_i - \bar{u}_j^{\text{LES}} * \bar{u}_i^{\text{LES}}) + \underline{\underline{l}}^{2D} \underline{\underline{\mathcal{M}}}_{ij}). \quad (40)$$

There is no spectrally sharp way to implement this type of deconvolution. Various non-equivalent procedures are possible in principle. Schmidt et al. (2008) describe a particular approach that is adopted here with a technical modification that improves its behavior near walls. To summarize, although the inverse operator  $l^{-1}$  arises as a natural and necessary consequence of the XLES ansatz, the ansatz per se does not uniquely define its meaning nor guarantee that it can be specified in a way that is free of unintended artifacts.

### 3.2. XLES: Consistency Preservation and ‘LES limit’

Both, the XLES mass conservation in section 2.2.3 and the coupling terms in section 2.2.1 and 2.2.2 assume the 3D large scale velocity field to be consistent, meaning each XLES-grid  $k$  contains the identical 3D large scale velocity field:  $\bar{u}_i^{\text{LES}} = \bar{u}_{k,i}^{\text{LES}} \equiv [l_k] \hat{u}_{k,i}$ .

In the XLES-vector notation this condition can be written as:

$$\underline{\underline{l}}^{1D} \hat{u}_i = \bar{u}_i^{\text{LES}} = \bar{u}_i^{\text{LES}} \begin{pmatrix} 1 \\ 1 \\ 1 \end{pmatrix} \quad (41)$$

with the 1D filter matrix defined in Eq. (11). This means consistency preserving terms should be independent of the XLES-grid  $k$ .

We assume that the initial conditions are consistent (this can easily be achieved) and need to prove a consistency preserving XLES-advancement including advective and diffusive terms and the sub-grid modeling.

The ‘directly resolved’ advection terms themselves ( $\partial_{x_j} \hat{u}_j * \hat{u}_i$ ) are violating the consistency condition, but by including the corresponding coupling (indirectly resolved terms):  $\partial_{x_j} \hat{u}_j * \hat{u}_i + \underline{\underline{\mathcal{X}}}_{ij}^{\text{XLES}}$ , the consistency is preserved. The same is valid for microscale terms and their couplings:  $\underline{\underline{l}}^{2D} \underline{\underline{\mathcal{M}}}_{ij} + \underline{\underline{l}}^{\dagger a} * \underline{\underline{C}} \underline{\underline{l}}^{2D} \underline{\underline{\mathcal{M}}}_{ij}$ .

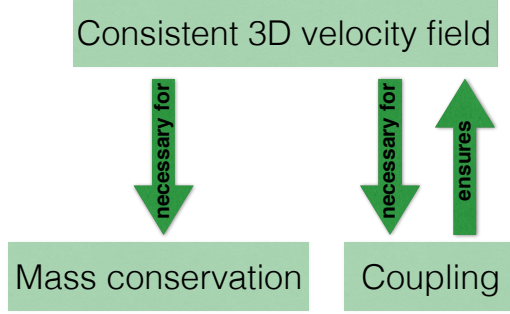


Figure 3: On the one hand the consistency preservation is invoked before the advection step to define the coupling terms. On the other hand the coupling guarantees the consistency to be still preserved after the advection step.

By rearranging the XLES advection terms and their corresponding couplings, we find:

$$\hat{u}_j * \hat{u}_i + \mathcal{X}_{ij}^{\text{XLES}} = \bar{u}_j * \bar{u}_i \quad (42)$$

with  $\bar{u}_{k,i} = [l_1 l_2 l_3 + s_1 l_2 l_3 + l_1 s_2 l_3 + l_1 l_2 s_3] u_i$ , which is equal in all XLES-grids  $k$ .

The same holds for the XLES sub-grid terms  $\underline{\underline{l}}^{2D} \underline{\underline{M}}_{ij}$  and their corresponding couplings  $\underline{\underline{l}}^{\dagger a} * \underline{\underline{C}} \underline{\underline{l}}^{2D} \underline{\underline{M}}_{ij}$  (proof by insertion).

In consequence the coupling terms are essential for a consistent 3D velocity field within XLES, as illustrated in figure 3.

In the implementation of XLES we check that the 3D large scale velocity field is still consistent every 100 timesteps to avoid numerical errors violating consistency preservation. All computations show the consistency to be limited by the floating point accuracy.

In the limit  $N_{\text{RSS}} \rightarrow N_{\text{LES}}$  the 2D filtered XLES-U equations collapse to the 3D filtered LES-U equations in each XLES-grid, because the RSS velocities vanish:  $\tilde{u}_i = \hat{u}_i - \bar{u}_i^{\text{LES}} = 0$

For  $N_{\text{LES}} \rightarrow N_{\text{RSS}} (\geq N_{\text{DNS}})$  in each direction, all velocity scales are resolved by the 3D grid and XLES-U (and LES-U) converges to DNS.

Within the ODT model, applied as an SGM in part II (Glawe et al. (2015)), all turbulent events are suppressed in the DNS-limit. Thus DNS is also a distinguished limit of ODTLES.

### 3.3. XLES: Coupled Advection Scheme

The characteristic shape of the XLES-grids (figure 1b–1d) is considered when choosing the numerical schemes to be implemented, e.g. an implicit time discretization in the highly resolved direction is applied, while explicit time schemes are used to advect large scale properties. Therefore different numerical advection schemes are mixed due to the XLES coupling terms, because the same property, represented by several XLES-grids is simultaneously advanced by different numerical schemes. Additionally the coupling requires a deconvolution function, which interacts with these numerical schemes.

In this section we present the numerical properties of this coupled advection scheme. For simplicity the 3D large scale velocity fields  $\overline{u}_i^{\text{LES}}$  are resolved by  $N_{\text{LES}}$  cells in each direction. The resolved small scale (RSS) properties are discretized with  $N_{\text{RSS}}$  cells in all XLES-grids.

The coupled advection scheme numerically approximates the equation

$$0 = (\underline{\mathbb{1}} - \underline{\delta}_i) \left( \partial_t \hat{u}_i + \sum_{j=1}^3 \partial_{x_j} \hat{u}_j * \hat{u}_i + \sum_{j=1}^3 (\underline{l}^\dagger * \underline{C} \partial_{x_j} (\hat{u}_j * \hat{u}_i - \overline{u}_j^{\text{LES}} * \overline{u}_i^{\text{LES}})) \right) \quad (43)$$

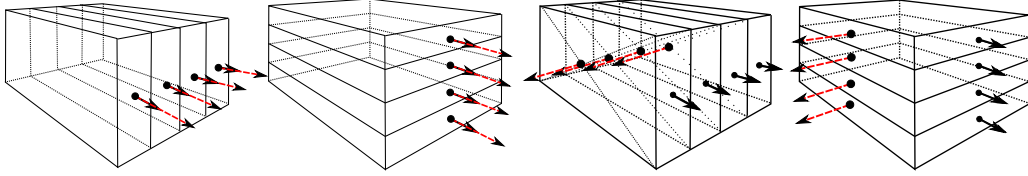
(according to Eq. (38); SGS terms are not considered).

Fundamental properties of the coupled advection scheme, e.g. the numerical dissipation and dispersion, can be demonstrated by solving a one dimensional linear advection problem. Then a constant wave speed  $c_j$  replaces the advecting velocities in Eq. (43):  $\hat{u}_j = \overline{u}_j^{\text{LES}} = c_j (1 \ 1 \ 1)^T$ . In this section the linearized coupled advection scheme is investigated, while the full non-linear coupled advection scheme is studied in section 3.4.

W.l.o.g. the advected velocity  $\underline{u}_1$  is represented by the two staggered XLES-grids containing  $\hat{u}_{2,1}$  and  $\hat{u}_{3,1}$  respectively while  $\hat{u}_{1,1}$  is evaluated using Eq. (36).

Two situations occur (see figure 4), as discussed here by a concrete example (generalization to other indices is trivial):

- Case 1:  $j = i \stackrel{w.l.o.g.}{=} 1$  in Eq. (43): Advection into  $x_1$ -direction; In both XLES-grids 2 and 3 the advection is coarsely resolved with  $N_{\text{LES}}$  grid cells.
- Case 2:  $2 \stackrel{w.l.o.g.}{=} j \neq i \stackrel{w.l.o.g.}{=} 1$  in Eq. (43): Advection into direction  $x_2$ ; In XLES-grid 2 the advection is resolved with  $N_{\text{RSS}}$  cells, respective with  $N_{\text{LES}}$  cells in XLES-grid 3.



(a) Case 1:  $j = i$  in Eq. (43). Coarsely resolved advection in XLES-grid 3 (left) and XLES-grid 2 (right). (b) Case 2:  $j \neq i$  in Eq. (43). Highly resolved advection in XLES-grid 3 (left) (coarsely) resolved advection in XLES-grid 3 (left) (XLES-grid 2 (right)).

Figure 4: XLES requires a coupled advection scheme. The advected velocity  $\hat{u}_i$  (bold arrows) is advected with the constant wave speed  $c_j$  (dashed arrows) and is resolved in two XLES-grids. For the two relevant cases the discrete staggered grids within one 3D large scale cell (compare to figure 1) are shown in (a) and (b).

To spatially discretize the advection terms, a central difference method (CDM) on a staggered grid is used.

Two different time discretizations are deployed:

- The highly resolved properties (using  $N_{\text{RSS}}$  cells) are discretized using a standard *2nd* order Crank-Nicolson (CN) scheme in time (see Crank and Nicolson (1996)). We will refer to this fully discrete scheme as CN-CDM.
- The coarse grained resolved properties (using  $N_{\text{LES}}$  cells) are discretized using a 3-stage *3rd* order TVD Runge-Kutta (RK3) scheme (see Spiteri and Ruuth (2002)). We will refer to this fully discrete scheme as RK3-CDM

The numerical properties of the numerical schemes without coupling are:

- The advection scheme CN-CDM is stable, dissipation free and has low dispersion.
- The RK3-CDM scheme is found to be stable, producing little dispersion and dissipation.

These properties transfer to the coupled advection schemes (in Cases 1 and 2).

Based on the expressions RK3-CDM and CN-CDM the coupled advection scheme in Case 1 (Case 2) is called RK3-RK3-CDM (CN-RK3-CDM).

To illustrate the coupling procedure w.l.o.g. for the CN-RK3-CDM scheme, we linearize and rewrite Eq. (43) in a semi-discrete form (in index notation). Hereby  $\hat{u}_{3,1}$  is discretized in XLES-grid 3 in Eq. (44) and  $\hat{u}_{2,1}$  in XLES-grid 2 in Eq. (45):

$$(\Delta t)\hat{u}_{3,1} = \int_{RK3} c_2 \partial_{x_2} \hat{u}_{3,1} dt \quad (44)$$

$$+ [l_3^{-1}][l_2] \left( \int_{CN} c_2 \partial_{x_2} \hat{u}_{2,1} dt - \int_{RK3} c_2 \partial_{x_2} \bar{u}_{2,1}^{LES} dt \right)$$

$$(\Delta t)\hat{u}_{2,1} = \int_{CN} c_2 \partial_{x_2} \hat{u}_{2,1} dt \quad (45)$$

$$+ [l_2^{-1}][l_3] \left( \int_{RK3} c_2 \partial_{x_2} \hat{u}_{3,1} dt - \int_{RK3} c_2 \partial_{x_2} \bar{u}_{3,1}^{LES} dt \right).$$

Here the numerical time discretizations of the advection terms are indicated (CN and RK3). The discrete coupling operators  $[l_k]$  and  $[l_k^{-1}]$  (see Eq. (7) and the algorithm described in section 3.1) are discretized by an explicit Euler scheme in time. Also the non-linear advection part which is not considered in the linear advection problem is discretized by an explicit Euler scheme in time.

The properties of the fully discrete linear coupled advection schemes are:

- The coupled advection scheme converges to the analytical solution for  $N_{LES} \rightarrow \infty$  as investigated in Appendix C.2 where the theoretical prediction e.g. by Tsai et al. (2002) is reproduced. This property is required to numerically realize the LES limit and DNS limit of XLES (section 3.2).
- The coupled advection scheme including the deconvolution (see section 3.1) reproduces well defined large scale behavior, even by simultaneously transporting small scale properties, as investigated in Appendix C.3.

The highly resolved CN-CDM scheme (using  $N_{RSS}$  cells) contributes to the coupled CN-RK3-CDM scheme (Case 2) and additionally increases the numerical accuracy of the coupled scheme. This is neither required for a well defined and converging XLES scheme nor the LES limit (or DNS limit) of XLES. As investigated in Appendix C.2 the highly resolved advection terms increase the coupled numerical accuracy up to a resolution ratio  $N_{RSS}/N_{LES} \lesssim$



10. With  $N_{\text{RSS}} \gtrsim 10N_{\text{LES}}$  the overall numerical error is dominated by the coarsely resolved RK3-CDM scheme.

The coupled numerical schemes, simultaneously discretized by multiple XLES-grids, are found to be appropriate for linear advection. Important numerical properties, like stability and dissipative behavior, transfer from the well known underlying numerical discretizations to the coupled advection scheme.

There are other time schemes, that possibly can be adapted to the special requirements of the XLES time advancement, e.g.:

- An IMEX (implicit/explicit) time scheme (see e.g. Cavaglieri and Bewley (2015) and references cited therein) applied to XLES can in principle lead to a high-order time integration for all terms (including non-linear advection and coupling), but to include the coupling terms into such a high order time scheme requires identical coefficients for the implicit and explicit integration terms.
- Adapting split-explicit schemes (see e.g. Gadd (1978)) to the XLES coupled advection can especially decrease the dispersive effects that arise.
- Large time step wave propagation schemes based on the work by LeVeque (1985) can perhaps improve the numerical properties of the applied CN scheme within the XLES advection scheme.

For the sake of completeness the diffusion terms are discretized by a central difference scheme in space with a first order explicit (implicit) Euler scheme in the coarse (fine) resolved XLES-grid direction.

### 3.4. XLES: Convergence of the XLES Approach

To verify the XLES model, we conduct a convergence study of XLES-U (unclosed XLES) for a fully developed turbulent flow, including the full diversity of non-linear advective effects: A turbulent channel flow with a friction Reynolds number  $Re_\tau = 395$  is computed. DNS results by Kawamura et al. (1999) (online available: Kawamura (2014)) are compared to the XLES-U outcome.

The DNS is resolved with  $N_{\text{DNS}} = 192$  non-equidistant cells in the horizontal direction (between the walls). For the spatial discretization a second order central difference scheme is used. The time is discretized using

a Crank-Nicolson scheme for the wall-normal non-linear terms and a second order Adams-Bashforth scheme for other terms (results for higher resolutions and higher order schemes are also available online). This numerical scheme is comparable to the XLES-U numerical scheme (see section 3.3).

For the XLES-U convergence study, the number of equidistant 3D large scale cells  $N_{\text{LES}}$  is increased using the values  $N_{\text{LES}} = \{16, 32, 64\}$  while  $N_{\text{RSS}} = 512$  is kept constant.

The time step size is limited by:

$$\Delta t = CFL \min_{i,k} \left( \frac{\Delta x_{k,i}^{\text{RSS}}}{\hat{u}_{k,i}} \right), \quad i, k = \{1, 2, 3\} \quad (46)$$

with a Courant-Friedrichs-Lewy number  $CFL = 0.45$  and the small scale cell size  $\Delta x_{k,i}^{\text{RSS}}$ .

To produce statistically significant results, the flow is averaged for  $t_{\text{ave}} \geq 25$  non-dimensional time units (compared to  $t_{\text{ave}} = 20$  for DNS) after reaching a statistically steady state.

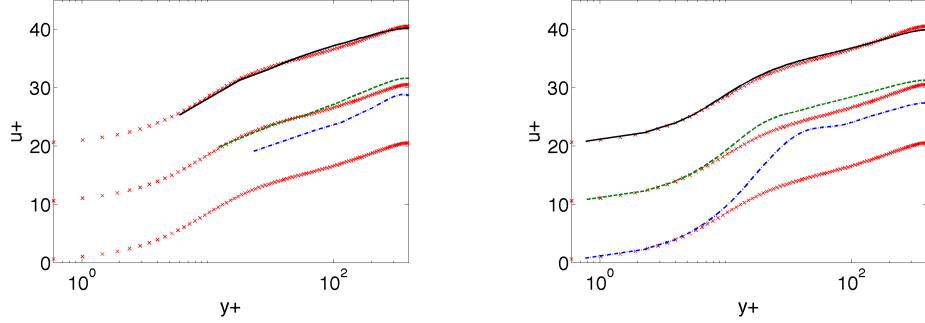
Additionally equidistant discretized LES-U (LES limit of XLES-U with  $N_{\text{RSS}} = N_{\text{LES}}$ , see section 3.2) channel flow results are compared to XLES-U. The latter resolves selected advective and diffusive small scale effects even without using a SGM. Those can be identified by comparing the XLES-U and LES-U channel flow results.

Figure 5 illustrates the results: The mean velocity profiles computed by XLES-U (see figure 5b) and LES-U (see figure 5a) are compared to DNS.

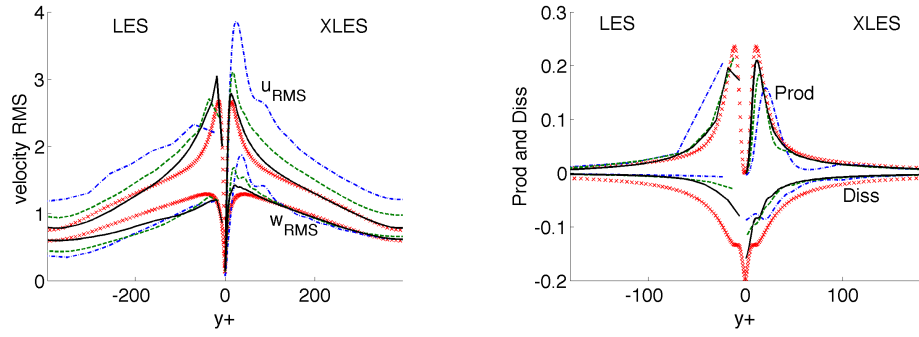
Additionally the streamwise and spanwise velocity RMSs (see figure 5c) and the budget terms of the turbulent kinetic energy (see figure 5d- 5f) are shown for XLES-U, LES-U, and DNS.

Both XLES-U and LES-U show convergence towards the DNS results with increasing 3D resolution. Following arguments in section 3.2 this implies the XLES error term  $\underline{\sigma}_{\text{XLES}}^{\text{spatial}}$  to be small. Additionally the XLES non-linear terms (and its LES limit) are sufficiently represented and converging, even if the under-resolved velocity profile (figure 5a and 5b) indicates noticeable numerical dissipation.

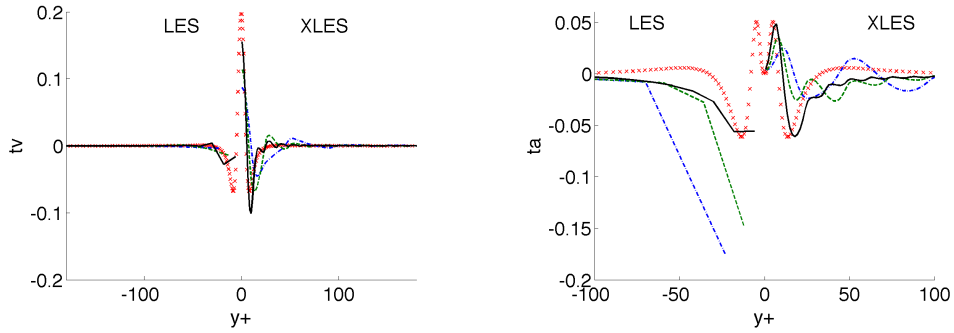
XLES-U is able to accurately represent diffusive effects, e.g. the laminar sublayer near the walls, independent of the 3D large scale resolution and reproduces basic advective effects including turbulence with  $N_{\text{LES}} \gtrsim 32$  3D cells for  $Re_\tau = 395$ . Additionally the turbulence statistics profit from the



(a) LES: law of the wall ( $\bar{u}_1^{\text{LES}}$ ). Profiles shifted with increasing  $N^{\text{LES}}$ . (b) XLES: law of the wall ( $\hat{u}_{2,1}$ ). Profiles shifted with increasing  $N^{\text{LES}}$ .



(c) Streamwise ( $u_{\text{RMS}}$ ) and spanwise ( $w_{\text{RMS}}$ ) velocity RMS. (d) Production (Prod) and Dissipation (Diss) of the turbulent kinetic energy.



(e) Viscous transport of the turbulent kinetic energy ( $tv$ ). (f) Advective transport of the turbulent kinetic energy ( $ta$ ).

Figure 5: Turbulent channel flow results for DNS (small crosses), LES-U, and XLES-U with  $N_{\text{LES}} = 16$  (dash-dotted),  $N_{\text{LES}} = 32$  (dashed), and  $N_{\text{LES}} = 64$  (solid). The XLES-U small scales are resolved using  $N_{\text{RSS}} = 512$  cells. XLES-U mean and statistical flow properties are based on the velocity field perpendicular to the channel walls  $\hat{u}_{2,i}$  (in the LES limit:  $\hat{u}_{2,i} = \bar{u}_i^{\text{LES}}$ ).

additional small scale effects represented by XLES compared to LES-U even with low 3D resolutions.

In part II (Glawe et al. (2015)) ODT is demonstrated to represent the turbulent effects not resolved by XLES-U, even with very coarse 3D resolutions (e.g.  $N_{\text{LES}} = 16$ ).

#### 4. Conclusions

In this work XLES, an extended LES model, is introduced. This approach is intended as a basis for a new class of turbulence models, tailored to describe a (XLES specific) macrostructure of highly turbulent flows including fully resolved molecular diffusion in domains of moderate complexity.

An innovative XLES filter strategy is derived, including a numerical representation of the resulting 2D filtered XLES equations by three coupled XLES-grids. This coupling requires a high order deconvolution function for 1D box filtered fields, wherefore a stabilized version of the algorithm introduced by Schmidt et al. (2008) is applied.

The 3D filtered LES-U (unclosed LES) equations and DNS are distinguished limits of XLES-U (unclosed XLES).

We verify the XLES-U equations:

- By analyzing the coupled (linear) advection scheme occurring in XLES.
- By performing a convergence study: The turbulent channel flow with  $Re_\tau = 395$  is compared to DNS and LES-U. Compared to LES-U low 3D resolutions are required in XLES-U to reproduce fundamental flow statistics, especially in the near wall region. E.g. the laminar sublayer is fully represented independently of the 3D resolution.

An XLES closure can be provided by the ODT model, which is able to capture the full turbulent cascade of highly turbulent flows, as introduced in part II (Glawe et al. (2015)). Recently Meiselbach (2015) introduces channel flow results up to  $Re_\tau = 600000$  using adaptive ODT by Lignell et al. (2013). This ODTLES model enables the representation of highly turbulent flows in domains of moderate complexity with coarse 3D resolutions basically independent of turbulent scales and at once represents diffusive and (turbulent) advective effects down to the molecular level using ODT. Hereby the 3D resolution needs to be sufficient to resolve the domain and possible secondary effects. E.g. due to secondary instabilities within a duct flow, the 3D

resolution indirectly depends on the Reynolds number (investigated in part II by Glawe et al. (2015)). The XLES model is especially advantageous for turbulent flows with crucial small scale effects, e.g. with important Prandtl or Schmidt number effects, buoyant stratification effects, or in the field of combustion.

In XLES a potential bottleneck in highly resolved incompressible simulations, the pressure handling, is only computed on a very coarse 3D grid and small scale pressure effects might be modeled. Closed XLES (e.g. ODTLES) is a promising and highly parallelizable approach to investigate fundamental atmospheric turbulent flows.

## Acknowledgments

The authors would like to thank H. Kawamura and colleagues for providing DNS results online (Kawamura (2014)). This work was supported by the Brandenburg University of Technology Cottbus-Senftenberg, the Helmholtz graduate research school GeoSim, and the Freie Universität Berlin.

## Appendix A. XLES: Vector Notation

We introduce an alternative to the vector notation in section 2 by writing the XLES velocity scales in index notation. The XLES vector  $\hat{u}_i$  includes the XLES vector elements  $\hat{u}_{k,i}$  represented in XLES-grids  $k$ ,  $k = \{1, 2, 3\}$ .

In index notation the resolved small scale (RSS) terms  $s_1 l_2 l_3$ ,  $l_1 s_2 l_3$ , and  $l_1 l_2 s_3$  can be expressed by one term:  $s_k l_{k \oplus 1} l_{l \oplus 2}$ , where  $\{k, k \oplus 1, k \oplus 2\}$  is a positive permutation of  $\{1, 2, 3\}$  (the 1D filter operators are commutable). The operator  $\oplus$  denotes the positive permutation:

$$q \oplus x = ((q + x - 1) \bmod 3) + 2 \quad (\text{A.1})$$

for  $q = \{1, 2, 3\}$  and  $x = \{1, 2\}$  (valid in three dimensions).

The XLES resolved velocity scales (Eq. (12)) are written in index notation

(using the operator  $\oplus$ ):

$$\begin{aligned}
\bar{u}_i &= [l_1 l_2 l_3 + s_1 l_2 l_3 + l_1 s_2 l_3 + l_1 l_2 s_3] u_i \\
&= \left[ l_1 l_2 l_3 + \sum_{q=1}^3 s_q l_{q\oplus 1} l_{q\oplus 2} \right] u_i \\
&= \left[ \sum_{q=1}^3 (l_q l_{q\oplus 1} l_{q\oplus 2} + s_q l_{q\oplus 1} l_{q\oplus 2}) - 2l_1 l_2 l_3 \right] u_i.
\end{aligned} \tag{A.2}$$

The 3D large scale operator  $[l_1 l_2 l_3]$  in the last row of Eq. (A.2) can be expressed in terms of  $[l_q l_{q\oplus 1} l_{q\oplus 2} + s_q l_{q\oplus 1} l_{q\oplus 2}]$ :

$$\begin{aligned}
-2l_1 l_2 l_3 &= - \sum_{q=1}^3 (1 - \delta_{qk}) (l_q l_{q\oplus 1} l_{q\oplus 2}) \\
&= - \sum_{q=1}^3 (1 - \delta_{qk}) ((l_q l_q + l_q - l_q l_q) l_{q\oplus 1} l_{q\oplus 2}) \\
&= - \sum_{q=1}^3 (1 - \delta_{qk}) l_q (l_q l_{q\oplus 1} l_{q\oplus 2} + \underbrace{(1 - l_q)}_{=s_q} l_{q\oplus 1} l_{q\oplus 2})
\end{aligned} \tag{A.3}$$

with the Kronecker delta operator defined in Eq. (37).

Here an additional arbitrary index  $k = \{1, 2, 3\}$  is introduced. Eq. (A.3) is satisfied for  $k = 1$ ,  $k = 2$ , and  $k = 3$ . This index  $k$  spans the XLES vector.

Insertion of the 3D large scale operator (Eq. (A.3)) into the XLES resolved velocity scales (Eq. (A.2)) leads to:

$$\bar{u}_{k,i} = \left[ \sum_{q=1}^3 (1 - (l_q - l_q \delta_{qk})) (l_q l_{q\oplus 1} l_{q\oplus 2} + s_q l_{q\oplus 1} l_{q\oplus 2}) \right] u_i, \quad k = \{1, 2, 3\}. \tag{A.4}$$

This XLES resolved velocity  $\bar{u}_{k,i}$  reproduces exactly the XLES resolved velocity scales in Eq. (12) including the XLES coupling  $\underline{\underline{C}} \underline{\underline{s}}^{1D} \underline{\underline{l}}^{2D}$ . XLES is interpreted as approach filtering the Navier-Stokes equations by applying the operator  $[l_1 l_2 l_3 + s_1 l_2 l_3 + l_1 s_2 l_3 + l_1 l_2 s_3]$  compared to  $[l_1 l_2 l_3]$  in LES (see table 1).

## Appendix B. XLES Mass Conservation: Resolved Small Scales

Divergence-free XLES velocity fields  $\hat{u}_i$  are guaranteed, if the 3D large scale velocity field  $\bar{u}_i^{LES} = [l_k]\hat{u}_{k,i}$  fulfills three conditions (see section 2.2.3):

- Con.1:  $\bar{u}_{k,i}^{LES}$  is consistent ( $\bar{u}_i^{LES} = \bar{u}_{k,i}^{LES}$ )
- Con.2:  $\bar{u}_i^{LES}$  is divergence free, enforced by 3D standard approach.
- Con.3:  $[l_k]$  is a discrete 1D box filter (defined in Eq. (7)) in  $x_k$ -direction.

The XLES velocity fields  $\hat{u}_i$  are divergence free as proved within one 3D large scale cell of the size  $\Delta x_k$  in  $x_k$ -direction (operator  $\oplus$  is defined in Eq. (A.1)):

$$\begin{aligned}
0 &= \int_{-\frac{\Delta x_k}{2}}^{\frac{\Delta x_k}{2}} \sum_{j=1}^3 \partial_{x_j} (\bar{u}_{k,j}^{LES} + \check{u}_{k,j}) dx_k = \int_{-\frac{\Delta x_k}{2}}^{\frac{\Delta x_k}{2}} \sum_{j=1}^3 \partial_{x_j} \hat{u}_{k,j} dx_k \quad (\text{B.1}) \\
&= \int_{-\frac{\Delta x_k}{2}}^{\frac{\Delta x_k}{2}} \partial_{x_k} \hat{u}_{k,k} dx_k + \int_{-\frac{\Delta x_k}{2}}^{\frac{\Delta x_k}{2}} \partial_{x_{k\oplus 1}} \hat{u}_{k,k\oplus 1} dx_k + \int_{-\frac{\Delta x_k}{2}}^{\frac{\Delta x_k}{2}} \partial_{x_{k\oplus 2}} \hat{u}_{k,k\oplus 2} dx_k \\
&= \hat{u}_{k,k} \left( \frac{\Delta x_k}{2} \right) - \hat{u}_{k,k} \left( -\frac{\Delta x_k}{2} \right) + \partial_{x_{k\oplus 1}} \int_{-\frac{\Delta x_k}{2}}^{\frac{\Delta x_k}{2}} \hat{u}_{k,k\oplus 1} dx_k + \partial_{x_{k\oplus 2}} \int_{-\frac{\Delta x_k}{2}}^{\frac{\Delta x_k}{2}} \hat{u}_{k,k\oplus 2} dx_k \\
&\stackrel{\text{Con.3}}{=} \bar{u}_{k,k}^{LES} \left( \frac{\Delta x_k}{2} \right) - \bar{u}_{k,k}^{LES} \left( -\frac{\Delta x_k}{2} \right) + \partial_{x_{k\oplus 1}} \bar{u}_{k,k\oplus 1}^{LES} + \partial_{x_{k\oplus 2}} \bar{u}_{k,k\oplus 2}^{LES} \\
&= \int_{-\frac{\Delta x_k}{2}}^{\frac{\Delta x_k}{2}} \sum_{j=1}^3 \partial_{x_j} \bar{u}_{k,j}^{LES} dx_k \stackrel{\text{Con.1}}{=} \int_{-\frac{\Delta x_k}{2}}^{\frac{\Delta x_k}{2}} \sum_{j=1}^3 \partial_{x_j} \bar{u}_j^{LES} dx_k \stackrel{\text{Con.2}}{=} 0.
\end{aligned}$$

for each XLES-grid  $k = \{1, 2, 3\}$ . Here a staggered grid is used, leading to  $\hat{u}_{k,k} \left( \frac{\Delta x_k}{2} \right) = \bar{u}_{k,k}^{LES} \left( \frac{\Delta x_k}{2} \right)$  without additional interpolation.

This in particular means the resolved small scale (RSS) velocity fields  $\check{u}_j$  are divergence free by construction.

## Appendix C. XLES: Numerical Advection Scheme

The XLES equations are discretized using multiple, coupled XLES-grids. This discretization includes a coupled advection scheme, possessing uncertain numerical properties.

The coupled advection scheme is investigated and verified by computing a linear wave propagation. The initial condition

$$u_1 = \sin(4\pi x_1) \quad (\text{C.1})$$

and periodic boundary conditions are used. The number of cells for the resolved small scale fields  $N_{\text{RSS}}$  and the 3D large scale field  $N_{\text{LES}}$  are varied. The wave is propagated for 10 wavelengths ( $t = 5L/c_j$ ;  $L \equiv 1$ ; constant wave speed  $c_j$ ).

All calculations are done with a Courant-Friedrichs-Lewy number  $CFL = 0.45$  limiting the time step size

$$\Delta t = CFL \min_{i,k} \left( \frac{\Delta x_{k,i}^{\text{LES}}}{\hat{u}_{k,i}} \right), \quad i, k = \{1, 2, 3\}. \quad (\text{C.2})$$

Please note the non-linear problem in section 3.4 is limited to time steps based on  $\Delta x_{k,i}^{\text{RSS}}$  instead of  $\Delta x_{k,i}^{\text{LES}}$ , which is investigated in part II (Glawe et al. (2015)) in detail.

### *Appendix C.1. Coupled Advection Schemes: RK3-RK3-CDM and CN-RK3-CDM*

Zha and Lingamgunta (2003) showed that RK2-CDM (central difference in space and 2nd order Runge Kutta in time) is unstable, while RK4-CDM (4th order Runge Kutta in time) is stable and fully dissipation free.

We found the coupled advection schemes RK3-RK3-CDM (Case 1 in section 3.3) and CN-RK3-CDM (Case 2 in section 3.3) to be stable and slightly dispersive (see figure C.6). Additionally RK3-RK3-CDM is little dissipative. The difference between RK3-RK3-CDM and CN-RK3-CDM is not significant. With increasing 3D resolution ( $N_{\text{LES}}$ ) the dispersive behavior decreases (convergence).

### *Appendix C.2. Coupled Advection Scheme: High Small Scale Resolution*

Numerical convergence for the XLES coupled advection scheme is unconditionally obtained for increasing 3D resolution ( $N_{\text{LES}} \rightarrow \infty$ ). This is valid for both coupled schemes: RK3-RK3-CDM and CN-RK3-CDM.

The convergence for the CN-RK3-CDM scheme with increasing small scale resolution ( $N_{\text{RSS}} \rightarrow \infty$ ) and two choices of constant 3D resolution  $N_{\text{LES}} = \{16, 64\}$  is additionally investigated. This kind of numerical convergence is not required to ensure a well defined and converging XLES approach.



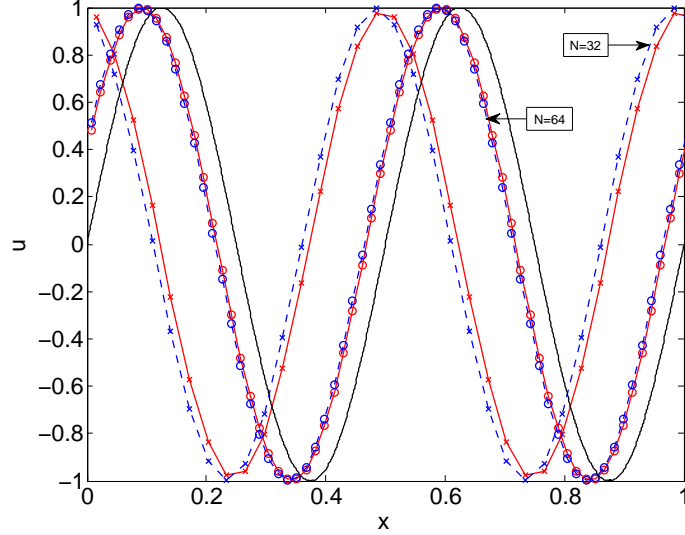


Figure C.6: A linear wave is propagated with constant velocity  $\hat{u}_j = \underline{c}_j$  over 10 wavelengths. The coupled numerical schemes CN-RK3-CDM (dashed) and RK3-RK3-CDM (solid) with  $N = N_{\text{RSS}} = N_{\text{LES}} = \{32, 64\}$  are shown. The black line is the analytical result.

A phase shift  $\Phi$  describes the numerical dispersion and thus measures the numerical accuracy (see figure C.7).

We find the numerical accuracy of the coupled advection scheme increasing up to a resolution ratio  $N_{\text{RSS}}/N_{\text{LES}} \lesssim 10$ . With higher ratios the numerical error of the coarse resolved scheme (RK3-CDM) dominates the coupled numerical error.

Thus the numerical accuracy is increased by increasing the resolved small scales within XLES up to some limit in addition to possibly resolving additional physical effects.

### Appendix C.3. Coupled Advection Scheme: Spectral Scale Separation

In this section the CN-RK3-CDM scheme demonstrates the preservation of (spectrally separated) large and small scale properties which are represented w.l.o.g. in XLES-grid 2.

A multi-scale wave with the initial condition

$$u_{2,1} = \sin(4\pi x_{2,1}) + 0.2 \sin(128\pi x_{2,1}) \quad (\text{C.3})$$

$$u_{3,1} = [l_3^{-1}][l_2]u_{2,1} = \sin(4\pi x_{3,1}) \quad (\text{C.4})$$

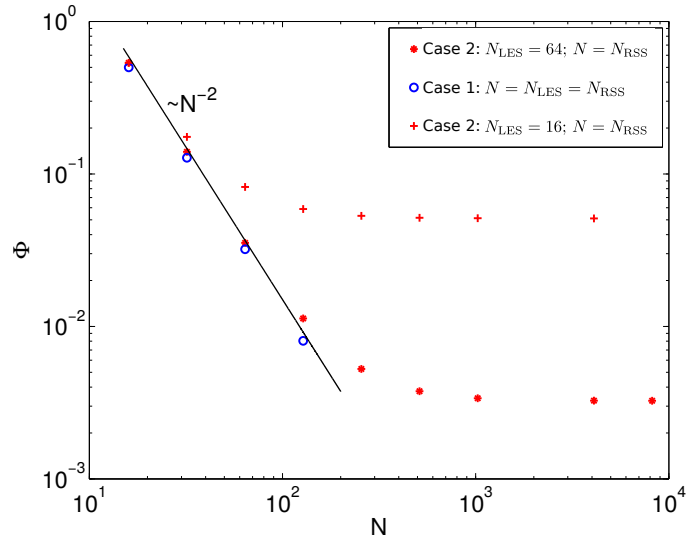


Figure C.7:  $\Phi$  is the phase difference between the analytical solution and the numerical result. Case 1: RK3-RK3-CDM scheme with  $N = N_{LES} = N_{RSS}$ . Case 2: CN-RK3-CDM scheme with  $N = N_{RSS}$  and  $N_{LES} = \{16, 64\}$ . For a CN-CDM scheme Tsai et al. (2002) analytically predict the behavior :  $\Phi \sim N^{-2}$ .

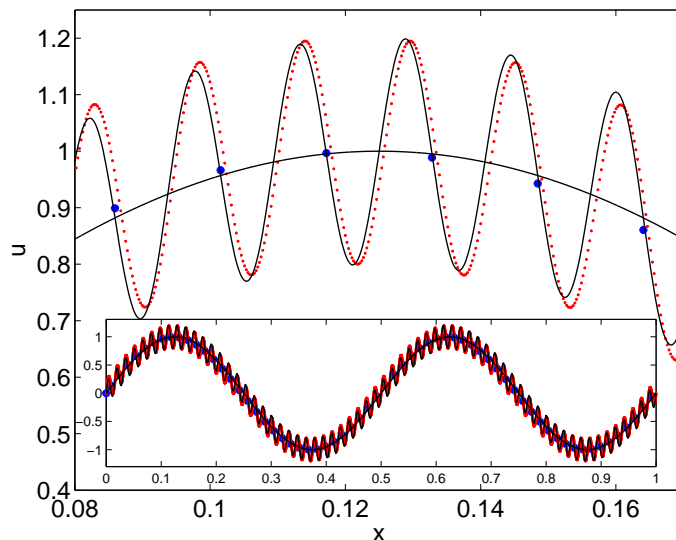


Figure C.8: A multi-scale wave with the initial condition in Eq. (C.3) (lines) propagates for 10 wavelengths. The full domain (small box) and one wave peak are shown. The **big points** corresponds to the 3D large scale field ( $N_{\text{LES}} = 64$  cells). The **small points** corresponds to the resolved small scales ( $N_{\text{RSS}} = 4096$ ). The black line corresponds to the analytical result.

is propagated for 10 wavelengths using  $N_{\text{LES}} = 64$  and  $N_{\text{RSS}} = 4096$  cells in the  $x_2$ -direction (advanced by Eq. (45) and (44)).

Note that the higher mode  $0.2 \sin(128\pi x_{2,1})$  is only resolved within XLES-grid 2 while XLES-grid 3 only captures the lower mode.

The box filtered and small scale properties are preserved, but little dispersed due to numerical effects (see figure C.8).

Burbeau, A., Sagaut, P., Bruneau, C.-H., 2001. A problem-independent limiter for high-order runge-kutta discontinuous galerkin methods. *J. Comput. Phys.* 169, 111 – 150.

Cao, S., Echehki, T., 2008. A low-dimensional stochastic closure model for combustion large-eddy simulation. *J. Turbul.* 9, 1–35.

Cavaglieri, D., Bewley, T., 2015. Low-storage implicit/explicit Runge–Kutta schemes for the simulation of stiff high-dimensional ODE systems. *J. Comput. Phys.* 286, 172–193.

- Crank, J., Nicolson, P., 1996. A practical method for numerical evaluation of solutions of partial differential equations of the heat-conduction type. *Adv. Comput. Math.* 6, 207–226.
- Ferziger, J., Peric, M., 1999. *Computational Methods for Fluid Dynamics*. Springer.
- Gadd, A. J., 1978. A split explicit integration scheme for numerical weather prediction. *Quarterly Journal of the Royal Meteorological Society* 104, 569–582.
- Germano, M., 1986. A proposal for a redefinition of the turbulent stresses in the filtered Navier-Stokes equations. *Phys. Fluids* 29, 2323–2324.
- Germano, M., Piomelli, U., Moin, P., Cabot, W. H., 1991. A dynamic sub-grid-scale eddy viscosity model. *Phys. Fluids A: Fluid Dynamics* 3, 1760–1765.
- Glawe, C., Schmidt, H., Kerstein, A., Klein, R., 2015. XLES part II: From extended large eddy simulation to ODTLES. submitted to *J. Comput. Phys.*
- Glawe, C., Schulz, F., Gonzalez-Juez, E., Schmidt, H., Kerstein, A., 2013. ODTLES simulations of turbulent flows through heated channels and ducts. In: *Proceedings of TSFP-8*. Poitiers, France.
- Gonzalez-Juez, E. D., Schmidt, R. C., Kerstein, A. R., 2011. ODTLES simulation of wall-bounded turbulent flows. *Phys. Fluids* 23, 125102.
- Kawamura, H., Dec. 2014. DNS database. <http://murasun.me.noda.tus.ac.jp/turbulence/index.html>, [Online; accessed Dec 2014].
- Kawamura, H., Abe, H., Matsuo, Y., 1999. DNS of turbulent heat transfer in channel flow with respect to Reynolds and Prandtl number effects. *Int. J. Heat Fluid Fl.* 20, 196–207.
- Kerstein, A. R., 1999. One-dimensional turbulence: Model formulation and application to homogeneous turbulence, shear flows, and buoyant stratified flows. *J. Fluid Mech.* 392, 277–334.

- Kerstein, A. R., Ashurst, W. T., Wunsch, S., Nilsen, V., May 2001. One-dimensional turbulence: Vector formulation and application to free shear flows. *J. Fluid Mech.* 447, 85–109.
- Lee, M., Moser, R. D., 2014. Direct numerical simulation of turbulent channel flow up to  $Re_\tau = 5200$ . under consideration for publication in *J. Fluid Mech.*
- Leonard, A., 1975. Energy cascade in large-eddy simulations of turbulent fluid flows. *Adv. Geophys.* 18, 237–248.
- LeVeque, R. J., 1985. A large time step generalization of godunovs method for systems of conservation laws. *SIAM J. Numer. Anal.* 22, 1051–1073.
- Lignell, D., Kerstein, A., Sun, G., Monson, E. I., 2013. Mesh adaption for efficient multiscale implementation of one-dimensional turbulence. *Theor. Comput. Fluid Dyn.* 27, 273–295.
- McDermott, R. J., 2005. Toward one-dimensional turbulence subgrid closure for large-eddy simulation. Ph.D. thesis, University of Utah.
- Meiselbach, F. T., 2015. Application of ODT to turbulent flow problems. Ph.D. thesis, BTU Cottbus-Senftenberg.
- Menon, S., Kerstein, A., 2011. The linear-eddy model. In: Echehki, T., Mastorakos, E. (Eds.), *Turbulent Combustion Modeling: Advances, New Trends and Perspectives*. Springer, pp. 221–247.
- Pope, S., 2000. *Turbulent Flows*. Cambridge University Press.
- Sagaut, P., 2006. *Large Eddy Simulation for Incompressible Flows: An Introduction*. Springer Verlag.
- Sannan, S., Weydahl, T., Kerstein, A. R., 2013. Stochastic simulation of scalar mixing capturing unsteadiness and small-scale structure based on mean-flow properties. *Flow Turbul. Combust.* 90, 189–216.
- Schmidt, R. C., Kerstein, A. R., McDermott, R., 2008. ODTLES: A multi-scale model for 3D turbulent flow based on one-dimensional turbulence modeling. *Comput. Methods Appl. Mech. Engrg.* 199, 865–880.

- Smits, A. J., Marusic, I., 2013. Wall-bounded turbulence. *Phys. Today* 66, 25–30.
- Spalart, P., Allmaras, S., 1992. A one-equation turbulence model for aerodynamic flows. In: 30th Aerospace Sciences Meeting and Exhibit. American Institute of Aeronautics and Astronautics.
- Spiteri, R. J., Ruuth, S. J., 2002. A new class of optimal high-order strong-stability-preserving time discretization methods. *SIAM J. Numer. Anal.* 40, 469–491.
- Tsai, T., Yang, J., Huang, L., 2002. Hybrid finite-difference scheme for solving the dispersion equation. *J. Hydraul. Eng.* 128, 78–86.
- Zha, G., Lingamgunta, C., 2003. On the accuracy of runge-kutta methods for unsteady linear wave equation. In: 41st Aerospace Sciences Meeting and Exhibit. American Institute of Aeronautics and Astronautics.